iopscience.iop.org

Home Search Collections Journals About Contact us My IOPscience

Engineering *p*–*n* junctions and bandgap tuning of InSe nanolayers by controlled oxidation

This content has been downloaded from IOPscience. Please scroll down to see the full text.

2017 2D Mater. 4 025043

(http://iopscience.iop.org/2053-1583/4/2/025043)

View the table of contents for this issue, or go to the journal homepage for more

Download details:

IP Address: 128.243.2.47
This content was downloaded on 10/05/2017 at 09:51

Please note that terms and conditions apply.

You may also be interested in:

Quantum Confinement and Photoresponsivity of -In2Se3 Nanosheets Grown by Physical Vapour Transport
Nilanthy Balakrishnan, Christopher R Staddon, Emily F Smith et al.

2D Materials Advances: From Large Scale Synthesis and Controlled Heterostructures to Improved Characterization Techniques, Defects and Applications
Zhong Lin, Amber McCreary, Natalie Briggs et al.

Photonics and optoelectronics of two-dimensional materials beyond graphene
Joice Sophia Ponraj, Zai-Quan Xu, Sathish Chander Dhanabalan et al.

Thickness-dependent carrier transport and optically-enhanced transconductance gain in III-VI multilayer InSe
Ching-Hwa Ho

Electronics and optoelectronics of quasi-1D layered transition metal trichalcogenides
Joshua O Island, Aday J Molina-Mendoza, Mariam Barawi et al.

Two-dimensional hexagonal semiconductors beyond grapheme
Bich Ha Nguyen and Van Hieu Nguyen

Van der Waals stacked 2D layered materials for optoelectronics
Wenjing Zhang, Qixing Wang, Yu Chen et al.

Photoluminescence of two-dimensional GaTe and GaSe films
O Del Pozo-Zamudio, S Schwarz, M Sich et al.

Synthesis, properties and applications of 2D non-graphene materials
Feng Wang, Zhenxing Wang, Qisheng Wang et al.

2D Materials

RECEIVED
22 November 2016

REVISED
3 February 2017

ACCEPTED FOR PUBLICATION
21 February 2017

PUBLISHED
8 March 2017

PAPER

Engineering *p–n* junctions and bandgap tuning of InSe nanolayers by controlled oxidation

Nilanthy Balakrishnan[1], Zakhar R Kudrynskyi[1], Emily F Smith[2], Michael W Fay[2], Oleg Makarovsky[1], Zakhar D Kovalyuk[3], Laurence Eaves[1], Peter H Beton[1] and Amalia Patanè[1]

[1] School of Physics and Astronomy, The University of Nottingham, Nottingham NG7 2RD, United Kingdom
[2] Nanoscale and Microscale Research Centre, The University of Nottingham, Nottingham NG7 2RD, United Kingdom
[3] Institute for Problems of Materials Science, The National Academy of Sciences of Ukraine, Chernivtsi Branch, Chernivtsi 58001, Ukraine

E-mail: nilanthy.balakrishnan@nottingham.ac.uk and amalia.patane@nottingham.ac.uk

Keywords: 2D materials, indium selenide, van der Waals crystals, indium oxide

Supplementary material for this article is available online

Abstract

Exploitation of two-dimensional (2D) van der Waals (vdW) crystals can be hindered by the deterioration of the crystal surface over time due to oxidation. On the other hand, the existence of a stable oxide at room temperature can offer prospects for several applications. Here we report on the chemical reactivity of γ-InSe, a recent addition to the family of 2D vdW crystals. We demonstrate that, unlike other 2D materials, InSe nanolayers can be chemically stable under ambient conditions. However, both thermal- and photo-annealing in air induces the oxidation of the InSe surface, which converts a few surface layers of InSe into In_2O_3, thus forming an InSe/In_2O_3 heterostructure with distinct and interesting electronic properties. The oxidation can be activated in selected areas of the flake by laser writing or prevented by capping the InSe surface with an exfoliated flake of hexagonal boron nitride. We exploit the controlled oxidation of *p*-InSe to fabricate *p*-InSe/*n*-In_2O_3 junction diodes with room temperature electroluminescence and spectral response from the near-infrared to the visible and near-ultraviolet ranges. These findings reveal the limits and potential of thermal- and photo-oxidation of InSe in future technologies.

1. Introduction

Stacking different two-dimensional (2D) van der Waals (vdW) crystals to form heterostructures is a new route to the fabrication of electronic devices [1–3]. Due to the numerous materials in the family of 2D vdW crystals, such as graphene, hexagonal boron nitride (hBN), metal dichalcogenides (MoS_2, $MoSe_2$, WS_2, etc), III-VI semiconductors (InSe, In_2Se_3, GaSe, GaTe, etc), and elemental semiconductors (black phosphorus, bP), a large and diverse variety of heterostructures are possible. This has already led to the successful fabrication of photodetectors, light emitting diodes, and high mobility field effect transistors [1, 2, 4–13]. Among these vdW crystals, γ-InSe, a direct-band gap semiconductor, is attracting increasing interest. Strong quantum confinement effects with decreasing layer thickness and high room temperature electron mobility (>0.1 m^2 V^{-1} s^{-1}) have been achieved in exfoliated InSe and/or films grown by physical vapour deposition [14–19]. Although the chemical stability of InSe has been questioned [20], recent research has shown that 2D InSe can be chemically inert under ambient conditions [21]. The chemical reactivity of the surface of a 2D material is very important as it can hinder the observation of novel phenomena and also impose constraints on device fabrication processes. For example, uncontrolled oxidation can compromise the use of multi-layer heterostructures in future technologies. On the other hand, as for silicon, the existence of stable oxides at room temperature can offer prospects for novel applications [22, 23]. Thermal annealing of bulk In-Se compounds in air or in an oxygen-rich environment can produce native oxides [24–27]. The formation and control of such oxides in 2D flakes has not yet been examined and can offer opportunities to fabricate novel 2D hybrid heterostructures.

Here we demonstrate that unlike several other 2D vdW crystals, such as GaSe and bP [28, 29], 2D InSe nanolayers can be chemically stable under ambient conditions over a period of several days. However, both

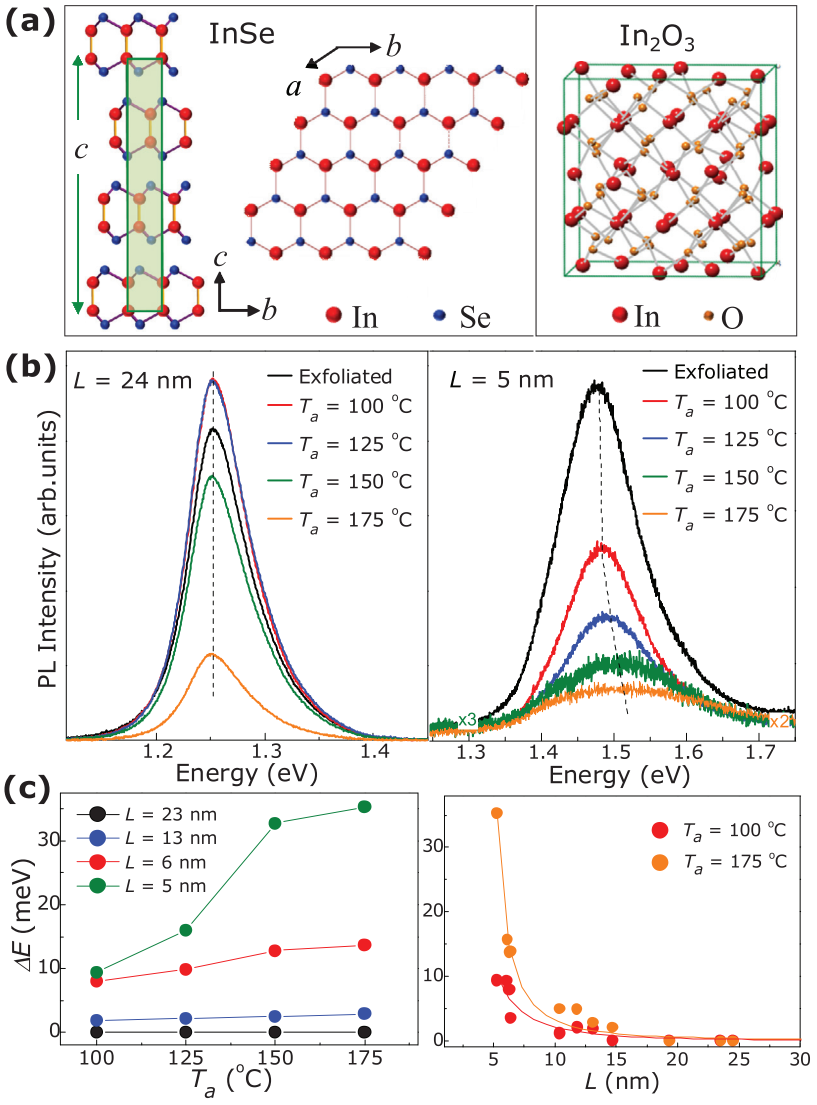

Figure 1. (a) Crystal structure of rhombohedral γ-InSe along the b–c plane and along the a–b plane (right), and of cubic (bixbyite) In_2O_3 (left). (b) Room temperature PL spectra of exfoliated p-InSe layers with different layer thicknesses L ($P = 0.1$ mW and $\lambda = 633$ nm). Spectra were measured following 1 h thermal annealing steps at increasing temperatures T_a. (c) T_a-dependence and L-dependence of the energy blue-shift ΔE of the PL emission. The continuous lines are guides to the eye.

thermal- and photo-annealing in air can induce an oxidation of the InSe surface over a short period of time, thus converting a few surface layers of InSe into In_2O_3. The propensity of InSe crystals of nanoscale thickness to oxidize in air at temperatures approaching ~100 °C or when illuminated with intense laser light is at first sight disadvantageous to future device applications; however, it can be turned to advantage by exploiting the optical transparency and electrically conducting properties of In_2O_3. Different thermal- and photo-annealing conditions can be used to control the thickness of the oxide layer and tune the bandgap of the non-oxidized 2D InSe by means of quantum confinement. The oxidation can be activated in selected areas of the flake by a focused laser beam or prevented by capping the InSe surface with a film of hBN. We exploit oxidation to fabricate InSe/In_2O_3 p–n junctions with functional properties including rectification, electroluminescence, and photoresponsivity from the near-infrared (NIR) to the visible (VIS) and ultraviolet (UV) ranges at room temperature. Our findings demonstrate the technological potential of InSe heterojunctions formed by surface oxidation. Oxidation of 2D InSe crystals could provide a platform for novel 2D heterostructures and also a route to the shielding of thin layers against contamination in air.

2. Results and discussion

Our samples were prepared from bulk Bridgman-grown rhombohedral γ-InSe. The primitive unit cell of γ-InSe has a lattice parameter $c = 24.961$ Å (along the c-axis) and contains three layers, each consisting of four closely-packed, covalently bonded, atomic sheets in the sequence Se–In–In–Se [30], see figure 1(a). Within each a–b plane, atoms form hexagons with lattice parameter $a = b = 4.002$ Å. The layers interact by weak van der Waals forces, resulting in anisotropic electronic properties. The InSe bulk layers are Cd-doped and have p-type conductivity with hole density $p = (8 \pm 3) \times 10^{13}\,cm^{-3}$ at $T = 300$ K, as derived from

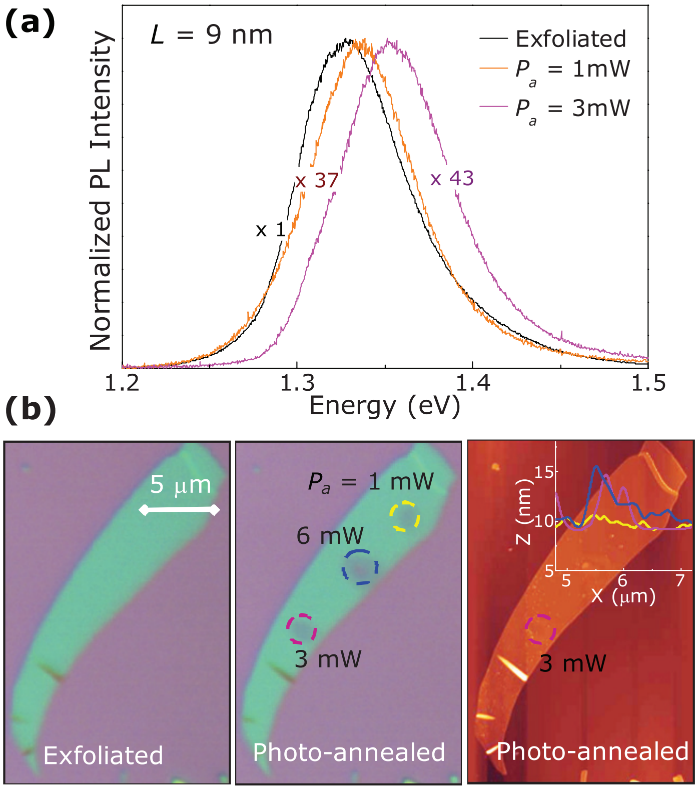

Figure 2. (a) Room temperature PL spectra of an InSe flake before and after laser exposure at different powers, P_a. (b) Optical image of the flake before (left) and after (right) laser exposure at powers $P_a = 1$ mW, 3 mW and 6 mW ($\lambda_a = 532$ nm, $t_a = 30$ mins). The circles indicate the laser-exposed areas of the flake. The image on the right is an AFM image of the flake after the laser exposure. The inset shows the AFM z-profiles of a laser-exposed areas.

Hall effect measurements [31, 32]. Flakes with areas from 1 to 10^3 μm^2 and thickness L from 4 to 100 nm were prepared from as-grown crystals by mechanical exfoliation using adhesive tape and deposited on SiO_2/Si substrates.

2.1. Thermal- and photo-oxidation of 2D γ-InSe

Room temperature ($T = 300$ K) PL spectra of exfoliated p-InSe flakes with different layer thickness L are shown in figure 1(b). Each PL spectrum was measured following a 1 h thermal annealing step in air at temperatures T_a ranging from 100 °C to 175 °C. The PL emission energy of freshly exfoliated flakes exhibits a large blue-shift with decreasing L, consistent with the quantum confinement of photo-excited carriers by the external surface of the flakes [14]. For flakes with $L > 15$ nm, the PL peak energy position is not affected by the annealing, although the PL intensity decreases significantly at $T_a > 150$ °C (figure 1(b)). In contrast, the PL emission of the thinner flakes exhibit an energy blue-shift, ΔE, with increasing T_a (figures 1(b) and (c)) and/or with increasing annealing time t_a (see supporting information S1 (stacks.iop.org/TDM/4/025043/mmedia)). For example, for flakes with $L = 5$ nm, the PL emission blue-shifts by up to $\Delta E = 35$ meV at $T_a = 175$ °C and $t_a = 1$ h (figure 1(b)). As shown in figures 2(a), a blue-shift of the PL emission energy can be also induced by a focused laser beam (beam diameter, $d \approx 1$ μm) with power $P_a > 1$ mW. The optical images of the flakes before and after laser exposure reveal a clear change of contrast around the laser exposed areas of the flake (see circled areas in figure 2(b)). This is accompanied by an increase of the flake thickness, as measured by AFM (figure 2(b)). We attribute the changes in the optical and structural properties of the annealed InSe layers to oxidation. As discussed below, the oxidation partially converts InSe into In_2O_3, thus modifying the confinement of the photo-generated carriers in the non-oxidized InSe layer. For an effective oxidation of the flakes to occur in air, the layers should be annealed to high temperatures ($T_a > 100$ °C) and/or relatively high laser power ($P_a > 0.5$ mW on a 1 μm diameter spot). In particular, at the highest laser powers examined in this work (>5 mW), oxidation can occur within a few seconds and fully quenches the PL emission. This deterioration of the optical properties at high laser powers is likely to arise from crystal defects in the oxide layer and/or at the interface with the InSe layer.

To explore these effects in detail, we use x-ray photoelectron spectroscopy (XPS), a sensitive technique that can probe the elemental and chemical composition of surfaces. High resolution XPS was performed on freshly exfoliated InSe layers, on InSe layers exposed to air under ambient conditions for up to 72 h, and on InSe layers annealed at $T_a = 175$ °C for $t_a = 1$ h. The high resolution spectra of the In 3d and Se 3d core levels are shown in figures 3(a) and (b), respectively. A peak model using pseudo-Voigt functions (sum of

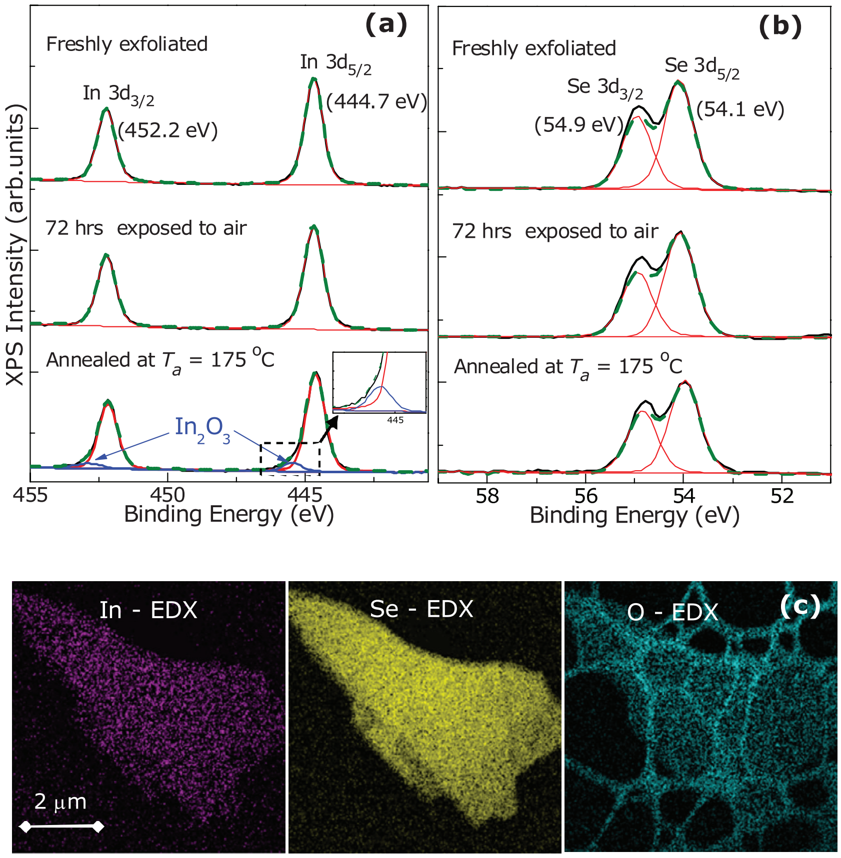

Figure 3. XPS spectra of In 3d (a) and Se 3d (b) core levels for freshly exfoliated *p*-InSe nanolayers (top), layers exposed to air for 72 h (middle) and layers annealed at $T_a = 175$ °C for $t_a = 1$ h (bottom). Red and blue curves are pseudo-Voigt functions (sum of 80%—Gaussian and 20%—Lorentzian) fitted (green curve) to the measured XPS spectra (black curve). (c) EDX maps of a *p*-InSe nanolayer exfoliated on a holey carbon grid thermally annealed at $T_a = 175$ °C ($t_a = 1$ h).

80%—Gaussian and 20%—Lorentzian) was fitted to the XPS spectra to distinguish contributions from different spin–orbit states and to identify the presence of metal oxides. The data and analysis confirm that detectable quantities of neither indium nor selenium oxides form when InSe is exposed to atmosphere. The binding energies of In 3d$_{5/2}$ ($E_{In} = 444.7 \pm 0.1$ eV) and Se 3d$_{5/2}$ ($E_{Se} = 54.1 \pm 0.1$ eV) are in good agreement with those in the literature for non-oxidized In-Se compounds [33–35]. They are not affected by exposure to air for over 72 h, indicating that the InSe nanolayers are stable under ambient conditions for several days. Moreover, the PL emission and Raman peaks of the exfoliated nanolayers persist for months when the flakes are stored in ambient conditions. We attribute the chemical stability of InSe to its high crystalline quality and low density of surface defects. Recent work has also shown that most ambient gases (e.g. H_2O, CO, CO_2, N_2, O_2) tend to interact weakly with InSe and that their bonding requires the presence of In and Se vacancies and/or Stone–Wales defects [21]. However, this behavior changes when the flakes are exposed to high temperatures. Following the annealing at $T_a = 175$ °C ($t_a = 1$ h), the high resolution XPS In 3d spectrum shows two additional peaks at $E_{In} = 445.4$ eV and 452.8 eV (figure 3(a)). These values correspond to the binding energy of In 3d reported in the literature for In_2O_3 [33, 36]. Similarly, In 4d spectra shows two additional peaks at $E_{In} = 18.3$ eV and 19.2 eV, which correspond to In_2O_3 (supporting information S2) [37]. We note that the XPS spectra show no evidence of selenium oxide (figure 3(b)). This suggests that Se tends to desorb from the surface, leaving behind nucleation sites for O-absorption. The oxidation process is also evident from additional complementary studies. As shown in figure 3(c), elemental energy dispersive x-ray (EDX) maps of thermally annealed ($T_a = 175$ °C and $t_a = 1$ h) InSe reveal a homogenous in-plane distribution of In, Se and O. Furthermore, transmission electron microscopy (TEM) studies of the heterostructures reveal the formation of the oxide layer and its crystal structure (supplementary information S4 and section 2.3).

2.2. Quantum confinement in InSe/In_2O_3 heterostructures

The formation of In_2O_3 at the expense of InSe changes the quantum confinement of the photogenerated carriers. To model the electronic properties of the InSe/In_2O_3 heterostructures, we examined the PL and AFM data for several flakes annealed in air under different conditions. As shown in figure 4(a), the room temperature PL peak energy, E_{2D}, of the freshly exfoliated *p*-InSe flakes is well described by a simple

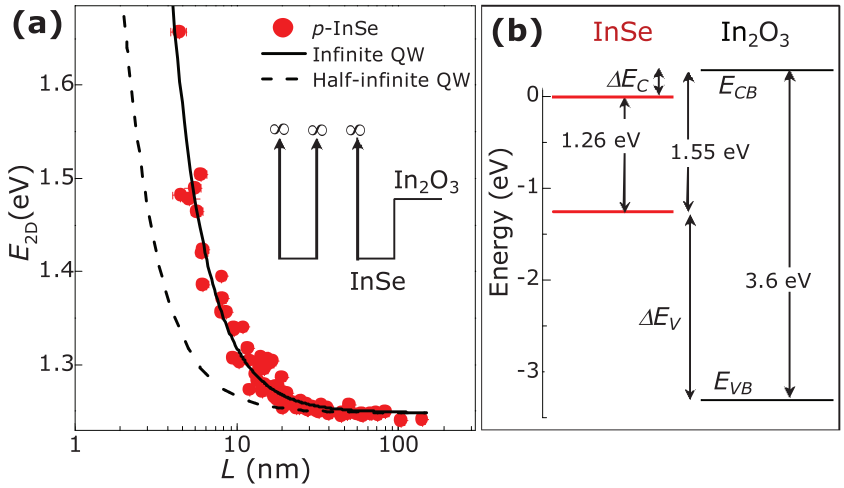

Figure 4. (a) Measured dependence on L of the peak energy, E_{2D}, of the PL emission at $T = 300$ K. The lines show the calculated dependence of E_{2D} for a quantum well (QW) with infinite potential barriers (continuous line) and half-infinite QW (dashed line) of width L at $T = 300$ K. The inset shows a schematic of infinite (left) and half-infinite (right) QW models. (b) Band diagrams for isolated InSe and In$_2$O$_3$ layers. Continuous horizontal lines indicate the band edges of the conduction and valence bands.

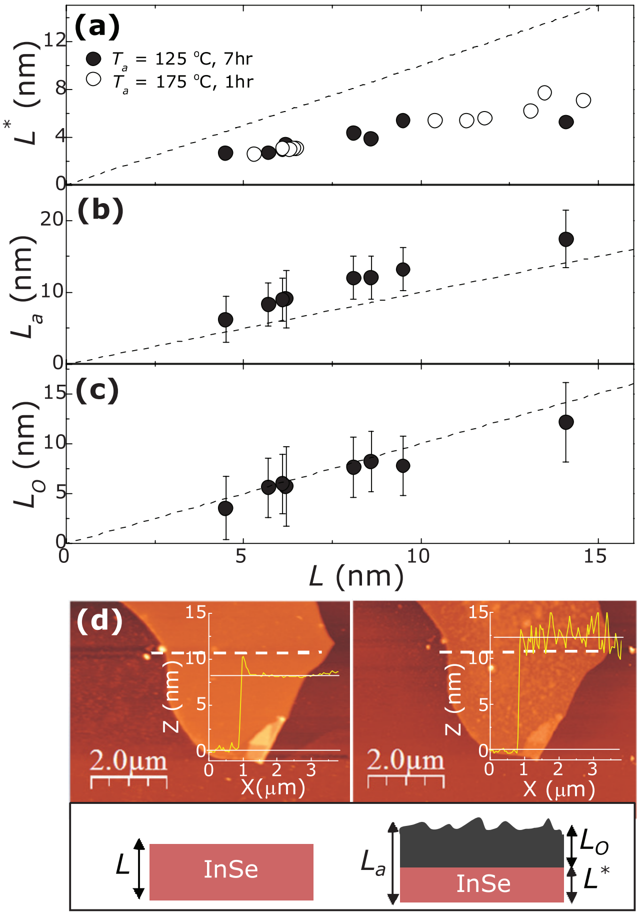

Figure 5. L-dependence of (a) the thickness, L^*, of the non-oxidized InSe layer estimated from a half-infinite quantum well model and the PL data; (b) the thickness, L_a, of the InSe/In$_2$O$_3$ flake measured by AFM; (c) the thickness of the oxide layer, L_o, calculated from (a) and (b). Full and empty dots are for $T_a = 125$ °C ($t_a = 7$ h) and $T_a = 175$ °C ($t_a = 1$ h), respectively. The dashed lines represent the thickness of the flake before annealing. (d) AFM image of an InSe flake before (left) and after (right) annealing at $T_a = 125$ °C ($t_a = 7$ h). The AFM z-profiles in the insets were obtained along the dashed line shown in the AFM images. The inset shows a schematic of an InSe flake before and after oxidation.

infinite square quantum well potential model, i.e. $E_{2D} = E_g - E_b + \pi^2\hbar^2/2L^2\mu_{\parallel c}$, where $E_g = 1.2635$ eV and $E_b = 0.015$ eV are the band gap energy and exciton binding energy for bulk InSe [38], $\mu_{\parallel c} = 0.054\, m_e$ is the electron–hole reduced mass for motion along the c-axis [14], and m_e is the electron mass in vacuum. The $E_{2D}(L)$ dependence for p-type InSe is similar to that reported previously for n-type InSe [14, 15]. Following

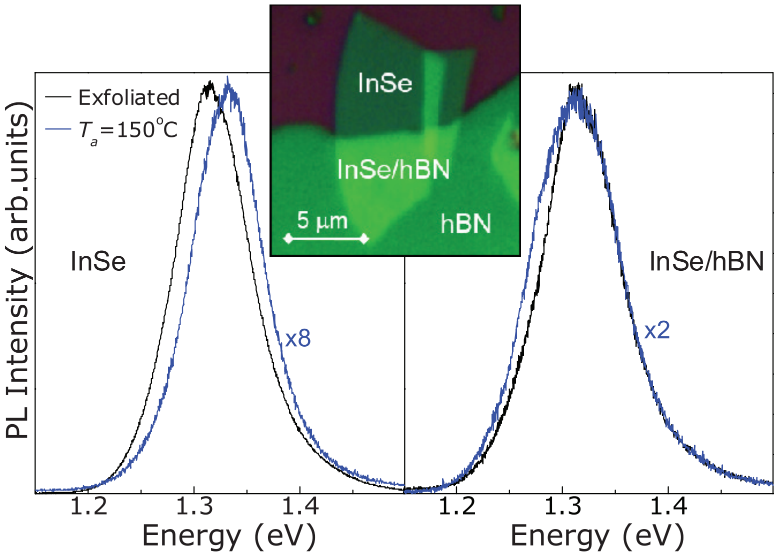

Figure 6. (a) Room temperature normalized PL spectra of *p*-InSe flakes with and without encapsulation by hBN ($P = 0.1$ mW and $\lambda = 633$ nm). Spectra were measured before (black line) and following (blue line) thermal annealing steps at increasing temperatures T_a up to 150 °C. The inset is an optical image showing the regions of the flake with and without the hBN film.

annealing, the thickness of the InSe layer is reduced and the air/InSe interface is replaced by In_2O_3/InSe, which we model as a half-infinite quantum well using the band alignment between In_2O_3 and InSe from [39] (dashed line in figure 4(a)). The conduction band (CB) minimum of In_2O_3 lies above that of InSe by $\Delta E_c = 0.29$ eV, whereas the valence band (VB) edge of In_2O_3 lies below the VB of InSe by $\Delta E_v = 2.05$ eV (figure 4(b)). Thus the oxide layer provides a lower potential barrier for electrons compared to that for non-oxidized InSe. By comparing the measured PL peak energy before and after annealing with the modeled curves, we can estimate the thickness, $L^* < L$, of the non-oxidized InSe.

Figure 5(a) shows the dependence of L^* on L for two different annealing conditions. It can be seen that L^* is reduced by about half the initial thickness L over a wide range of L from 4 nm to 14 nm (see also supporting information S3). From our estimate of L^* and the thickness L_a of the flake measured by AFM after annealing (figure 5(b)), we estimate the thickness L_o of the oxide layer, i.e. $L_o = L_a - L^*$ (figure 5(c)). For example, for the freshly exfoliated and annealed flake shown in figure 5(d), following annealing the thickness of the flake increases from $L \sim 8$ nm to $L_a \sim 12$ nm. The latter comprises the contribution of the non-oxidized InSe ($L^* \sim 4$ nm) and In_2O_3 ($L_a \sim 8$ nm) layers. Thus the oxide layer grows both down into the InSe flake and up out of it, with ~50% of the oxide thickness lying below the original surface and ~50% above it. Correspondingly, carriers experience a different confinement in the InSe/In_2O_3 heterostructure compared to the freshly exfoliated InSe, leading to an increase of the effective band gap energy by about 10 meV.

The energy shift of the PL emission depends on the annealing conditions and it is larger for thin flakes due to the stronger sensitivity of their band gap energy to the layer thickness (figure 4(a)). In general, the oxidation is accompanied by an increase of the surface roughness. Furthermore, crystalline defects that are present in the oxide and/or at the interface with InSe, can quench the PL signal. This effect is more pronounced as the electronic wave function spreads out into the In_2O_3 potential barrier, e.g. for thin layers and for annealing at high T_a and/or P_a.

We also investigated the effect of capping the InSe flakes with a layer of hexagonal boron nitride (hBN). As shown in figure 6, the oxidation of the InSe surface can be prevented by capping the flakes with a thin (~10 nm) hBN film: following thermal annealing, an energy shift of the PL emission is visible only on those areas of the InSe flakes that are not capped with hBN. Moreover, the PL intensity of the uncapped InSe decreases by a factor of 8. On the other hand, the PL intensity of the capped InSe decreases by only a factor of 2. We note that although hBN is strongly resistant to oxidation up to high temperatures (~800 °C) [40], following thermal- or photo-annealing the regions of InSe encapsulated by hBN show a reduction in PL intensity; this is likely caused by the formation of crystal defects at the InSe/hBN interface. Thus although hBN prevents the oxidation of InSe, it does not stop the degradation of the optical properties of InSe.

These results show that we can exploit the thermal- and photo-induced oxidation of InSe flakes in air to form InSe/In_2O_3 heterostructures (figures 1 and 2). By choosing appropriate annealing conditions, we can vary the thickness of the oxide and hence tune the bandgap of the non-oxidized InSe layer by means of quantum confinement (figures 4 and 5). The oxidation can be performed on selected areas of the InSe flakes by partially capping with a film of hBN or by a focused laser beam, which provides a tool to modify the band gap energy in the layer plane with micrometer spatial resolution (figure 2).

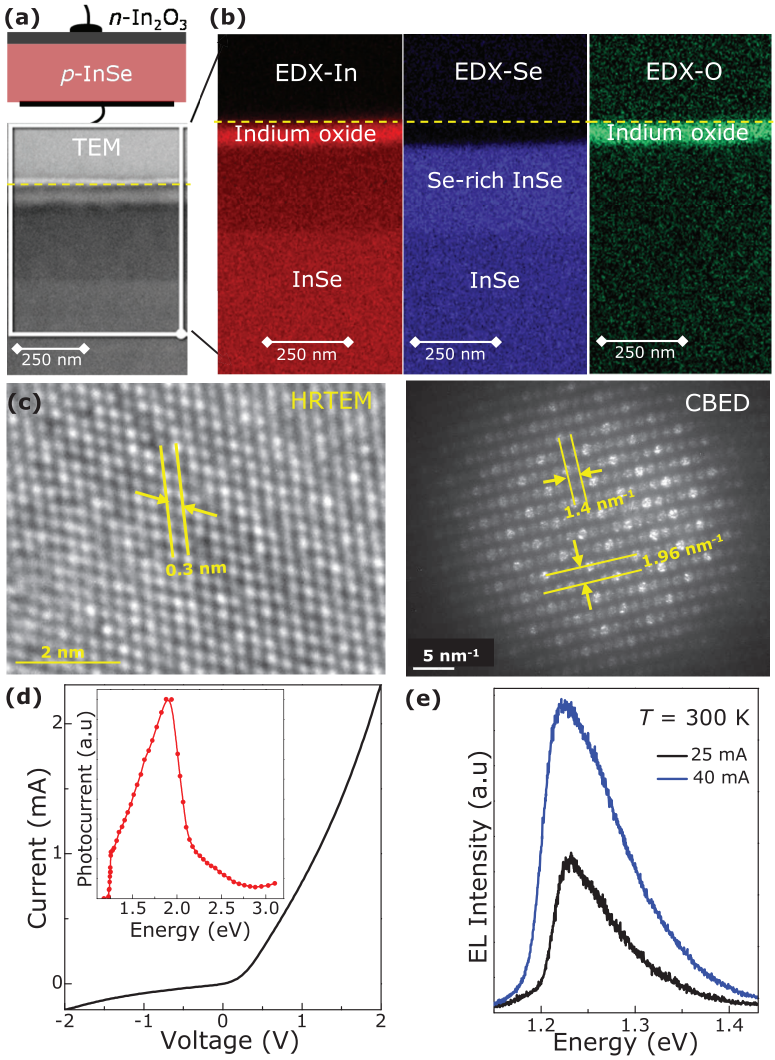

Figure 7. (a) Schematic diagram of the p-InSe/n-In$_2$O$_3$ junction and TEM image. (b) EDX maps of a cross-sectional area of the junction. The yellow lines show the top surface of In$_2$O$_3$. (c) HRTEM and CBED images of In$_2$O$_3$. (d) Current–voltage characteristics of the p-InSe/n-In$_2$O$_3$ junction at $T = 300$ K. The inset shows the photoconductivity spectrum at $T = 300$ K and $V = 0$ V. (e) Electroluminescence (EL) spectra at $T = 300$ K and current $I = 25$ mA and 40 mA.

2.3. Oxidation of *p*-type InSe for functional devices

The existence of a stable oxide on InSe and the selective oxidation of InSe offer the prospect for several technological applications. For the stable cubic (bixbyite) phase of In$_2$O$_3$, the primitive unit cell has a lattice parameter $a = 10.077$ Å (see figure 1(a)) [41]. In$_2$O$_3$ has n-type conductivity due to the excess of In-atoms and oxygen vacancies, both of which act as donors. It is also transparent over a wide spectral range with a band gap energy $E_g = 3.6$ eV at $T = 300$ K [39]. These properties, in combination with those of p-type InSe, can be used to design and fabricate different types of heterostructures, including rectifying p–n junctions and light emitting diodes. To fabricate the p–n junctions, bulk flakes of p-InSe with area of ~5×5 mm^2 and thickness of ~1 mm were annealed in air at $T_a = 450$ °C for $t_a = 96$ h. These annealing conditions were chosen to form a thick conducting oxide layer. Following annealing, indium ohmic contacts were formed on the top In$_2$O$_3$ and bottom InSe layers.

Figures 7(a) and (b) illustrates cross-sectional transmission electron microscopic (TEM) and EDX images of a p-InSe/n-In$_2$O$_3$ junction. The TEM image and the EDX elemental maps reveal an In$_2$O$_3$ layer of thickness $L_o \approx 75$ nm. The interface of In$_2$O$_3$ with InSe is not atomically abrupt and comprises an intermediate layer containing an excess of Se-atoms, but no oxygen (i.e. In ~ 43% and Se ~ 57%). The high resolution TEM (HRTEM) and convergent beam electron diffraction (CBED) images of the In$_2$O$_3$ layer (figure 7(c)) reveal that In$_2$O$_3$ is crystalline. We estimate interplanar spacings of 0.3 nm, 0.51 nm and 0.71 nm, which correspond to the (2 2 2), (0 0 2) and (1 1 0) crystal planes of cubic-In$_2$O$_3$. Additional HRTEM and CBED images for the Se-rich regions and InSe layers are shown in the the supporting information S4.

The room temperature current–voltage characteristics, I–V, of the junction diodes show rectification, see figure 7(d). The inset of figure 7(d) shows the room temperature photocurrent spectrum of the junction diode at zero bias ($V = 0$ V) and reveals a broad-band spectral sensitivity from the NIR to the VIS and UV ranges. The absorption edge is at a photon energy ($h\nu$ ~ 1.25 eV) corresponding to the calculated excitonic absorption in bulk γ-InSe at $T = 300$ K. We attribute the cut-off at $h\nu \sim 3$ eV to the photon absorption in the oxide: the high energy incident photons are mostly absorbed near the surface where the recombination time is short and photocarriers recombine before being collected at the junction interface. For white light excitation of power 100 mW cm^{-2}, the junctions produce an open-circuit voltage $V_{oc} \sim 0.6$ V and a short-circuit current density $J_{sc} \sim 30$ mA cm^{-2} at room temperature, corresponding to a conversion efficiency of 6%. The p–n junction also operates as light-emitting diode at room temperature. Figure 7(e) shows typical room temperature electroluminescence (EL) emission spectra. The EL emission is peaked close to the band gap energy of γ-InSe and redshifts with increasing current due to lattice heating. These results demonstrate the potential of the bipolar character of these heterostructures for technological applications.

3. Conclusion

Our data and analysis demonstrate that InSe nanolayers can be chemically stable under ambient conditions for several days. The high chemical stability of InSe differs from the behavior reported for numerous 2D van der Waals crystals, including other metal chalcogenide layered compounds. Furthermore, thermal- and photo-annealing in air can be used to induce the oxidation of the InSe surface, resulting in a reduction of the InSe layer thickness. Correspondingly, carriers experience a different quantum confinement in the InSe/In_2O_3 heterostructure from the case of simple InSe nanolayers. This leads to a change of the band gap energy relative to that of freshly exfoliated InSe. However, crystalline defects that are present in the oxide and/or at the interface with InSe, can quench the optical signals. The measured reduction of the PL intensity is an unwanted side effect of the oxidation, which nevertheless does not prevent the fabrication of working devices. The oxidation can be activated in selected areas of the flake by a focused laser beam or prevented by capping the InSe surface with hexagonal boron nitride. To test the potential of oxidation for applications, we have fabricated p-InSe/n-In_2O_3 junctions with functional properties including rectification, electroluminescence emission, and broad band photoresponsivity at room temperature. These findings reveal the limits and potential of thermal- and photo-oxidation of InSe nanolayers, and are relevant to exploitation of InSe in future technologies.

4. Methods

The bulk InSe crystals were grown by the Bridgman method at the Institute for Problems of Materials Science, The National Academy of Sciences of Ukraine, Chernivtsi Branch, Ukraine. The as-grown InSe crystals were studied by x-ray diffraction (XRD) using a DRON-3 x-ray diffractometer with a monochromatic Cu-Kα radiation of wavelength $\lambda = 1.5418$ Å. The XRD data revealed that the InSe crystal had γ-phase structure. For the XPS studies InSe flakes (areas from 1 to 10^3 μm^2) were exfoliated on 7 × 7 mm^2 SiO_2/Si substrates. The XPS measurements were performed using a Kratos AXIS ULTRA with a monochromatic Al Kα x-ray source ($h\nu = 1486.6$ eV) operated at 10 mA emission current and 12 kV anode potential ($P = 120$ W), and the data processing was performed using CASAXPS version 2.3.17PR1.1 software with Kratos sensitivity factors (RSFs) to determine atomic% values from the peak areas. The electron collection spot size is $\sim 700 \times 300$ μm^2. All XPS binding energies were calibrated with respect to the C 1s peak at a binding energy of 284.8 eV. For the transmission electron microscopy (TEM), convergent beam electron diffraction (CBED), and energy-dispersive x-ray (EDX) studies, a cross-sectional sample of the junction was prepared by Ga ion beam thinning, with a protective Pt layer deposited on the region of interest to prevent damage of the structure during ion beam milling and lift-out in an FEI Quanta 3D FIB-SEM equipped with an Omniprobe micromanipulator system. TEM analysis was performed in a JEOL JEM-2100Plus equipped with an Oxford Instruments XMax 100TLE EDX detector and a JEOL JEM 2100F equipped with an Oxford Instruments XMax 80 EDX detector.

The experimental set-up for μPL and μEL measurements comprised a He–Ne laser ($\lambda = 633$ nm) and a frequency-doubled Nd:YVO_4 laser ($\lambda = 532$ nm), an XY linear positioning stage, an optical confocal microscope system, a spectrometer with 150 and 1200 groves mm^{-1} gratings, equipped with a charge-coupled device and a liquid-nitrogen cooled (InGa)As array photodetector. The laser beam was focused to a diameter $d \approx 1$ μm using a 100 × objective and the μPL spectra were measured at low power ($P \sim 0.1$ mW) to avoid lattice heating. For the photoconductivity studies, light from a quartz halogen lamp, dispersed through a MDR-23 diffraction grating monochromator, and modulated with a mechanical chopper, was focused onto the junction. The photocurrent signal was measured using a standard lock-in amplification technique. Images of the InSe layer topography were acquired by AFM in tapping mode under ambient conditions.

Acknowledgment

This work was supported by the Engineering and Physical Sciences Research Council (EPSRC) (under grants EP/M012700/1 and EP/K005138/1, and EPSRC-funding for strategic equipment), the Horizon 2020 Graphene Flagship Project 604391, The University of Nottingham, and The National Academy of Sciences of Ukraine.

Supplementary data

Supporting information available: Photo-annealing studies at constant laser power, x-ray photoelectron spectroscopy (XPS) of InSe nanolayers, time-dependent thermal annealing studies at constant temperature, high resolution transmission electron microscopic (HRTEM) and convergent beam electron diffraction (CBED) images of p-InSe/n-In$_2$O$_3$ junction device and a table of electron and hole effective masses of InSe and In$_2$O$_3$ for motion along the c-axis. This material is available free of charge via the Internet at http://iopscience.iop.org/. The data, including images and spectroscopic measurements, on which this manuscript was based are available as an online resource with digital object identifier 10.17639/nott.73.

References

[1] Novoselov K S, Mishchenko A, Carvalho A and Neto A H C 2016 2D materials and van der Waals heterostructures *Science* **353** aac9439

[2] Zhang W, Wang Q, Chen Y, Wang Z and Wee A T S 2016 van der Waals stacked 2D layered materials for optoelectronics *2D Mater.* **3** 22001

[3] Koda D S, Bechstedt F, Marques M and Kühl Teles L 2016 Coincidence lattices of 2D crystals: heterostructure predictions and applications *J. Phys. Chem.* C **120** 10895–908

[4] Avsar A, Vera-Marun I J, Tan J Y, Watanabe K, Taniguchi T, Castro Neto A H and Özyilmaz B 2015 Air-stable transport in graphene-contacted, fully encapsulated ultrathin black phosphorus-based field-effect transistors *ACS Nano* **9** 4138–45

[5] Balakrishnan N, Kudrynskyi Z R, Fay M W, Mudd G W, Svatek S A, Makarovsky O, Kovalyuk Z D, Eaves L, Beton P H and Patanè A 2014 Room temperature electroluminescence from mechanically formed van der Waals III–VI homojunctions and heterojunctions *Adv. Opt. Mater.* **2** 1064–9

[6] Buscema M, Island J O, Groenendijk D J, Blanter S I, Steele G A, van der Zant H S and Castellanos-Gomez A 2015 Photocurrent generation with two-dimensional van der Waals semiconductors *Chem. Soc. Rev.* **44** 3691–718

[7] Georgiou T *et al* 2012 Vertical field-effect transistor based on graphene–WS$_2$ heterostructures for flexible and transparent electronics *Nat. Nanotechnol.* **8** 100–3

[8] Koppens F H, Mueller T, Avouris P, Ferrari A C, Vitiello M S and Polini M 2014 Photodetectors based on graphene, other two-dimensional materials and hybrid systems *Nat. Nanotechnol.* **9** 780–93

[9] Mudd G W *et al* 2015 High broad-band photoresponsivity of mechanically formed InSe-graphene van der Waals heterostructures *Adv. Mater.* **27** 3760–6

[10] Petrone N, Chari T, Meric I, Wang L, Shepard K L and Hone J 2015 Flexible graphene field-effect transistors encapsulated in hexagonal boron nitride *ACS Nano* 8953–9

[11] Tielrooij K J, Piatkowski L, Massicotte M, Woessner A, Ma Q, Lee Y, Myhro K S, Lau C N, Jarillo-Herrero P, van Hulst N F and Koppens F H L 2015 Generation of photovoltage in graphene on a femtosecond timescale through efficient carrier heating *Nat. Nanotechnol.* **10** 437–43

[12] Zhang W *et al* 2014 Ultrahigh-gain photodetectors based on atomically thin graphene-MoS$_2$ heterostructures *Sci. Rep.* **4** 3826

[13] Tamalampudi S R, Lu Y Y, Kumar U R, Sankar R, Liao C D, Moorthy B K, Cheng C H, Chou F C and Chen Y T 2014 High performance and bendable few-layered InSe photodetectors with broad spectral response *Nano Lett.* **14** 2800–6

[14] Mudd G W *et al* 2013 Tuning the bandgap of exfoliated InSe nanosheets by quantum confinement *Adv. Mater.* **25** 5714–8

[15] Bandurin D A *et al* 2016 High electron mobility, quantum Hall effect and anomalous optical response in atomically thin InSe *Nat. Nanotechnol.* https://doi.org/10.1038/NNANO.2016.242

[16] Brotons-Gisbert M *et al* 2016 Nanotexturing to enhance photoluminescent response of atomically thin indium selenide with highly tunable band gap *Nano Lett.* **16** 3221–9

[17] Balakrishnan N *et al* 2016 Quantum confinement in β-In$_2$Se$_3$ layers grown by physical vapour transport for high responsivity photodetectors *2D Mater.* **3** 1–8

[18] Sucharitakul S, Goble N J, Kumar U R, Sankar R, Bogorad Z A, Chou F C, Chen Y T and Gao X P A 2015 Intrinsic electron mobility exceeding 10^3 cm^2/(V s) in multilayer InSe FETs *Nano Lett.* **15** 3815–9

[19] Feng W, Zhou X, Tian W Q, Zheng W and Hu P 2015 Performance improvement of multilayer {InSe} transistors with optimized metal contacts *Phys. Chem. Chem. Phys.* **17** 3653–8

[20] Geim A K and Grigorieva I V 2013 van der Waals heterostructures *Nature* **499** 419–25

[21] Politano A, Chiarello G, Samnakay R, Liu G, Gürbulak B, Duman S, Balandin A A and Boukhvalov D W 2016 The influence of chemical reactivity of surface defects on ambient-stable InSe-based nanodevices *Nanoscale* **8** 8474–9

[22] Deal B E and Grove A S 1965 General relationship for the thermal oxidation of silicon *J. Appl. Phys.* **36** 3770–8

[23] Jaeger C R 2002 Introduction to microelectronic fabrication *Modular Series on Solid State Devices* ed G W Neudeck and R F Pierret (Englewood Cliffs, NJ: Prentice Hall) p 332

[24] Balitskii O A, Berchenko N N, Savchyn V P and Stakhira J M 2000 Characteristics of phase formation during indium selenides oxidation *Mater. Chem. Phys.* **65** 130–5

[25] Ho C H, Lin C H, Wang Y P, Chen Y C, Chen S H and Huang Y S 2013 Surface oxide effect on optical sensing and photoelectric conversion of alpha-In$_2$Se$_3$ hexagonal microplates *ACS Appl. Mater. Interfaces* **5** 2269–77

[26] Yuan Z, Zhu X, Wang X, Cai X, Zhang B, Qiu D and Wu H 2011 Annealing effects of In$_2$O$_3$ thin films on electrical properties and application in thin film transistors *Thin Solid Films* **519** 3254–8

[27] Katerynchuk V M and Kudrynskyi Z R 2013 Optical size effect in In$_2$O$_3$ nanostructured films *Semiconductors* **47** 345–8

[28] Del Pozo-Zamudio O *et al* 2015 Photoluminescence and Raman investigation of stability of InSe and GaSe thin films arXiv:1506.05619

[29] Edmonds M T, Tadich A, Carvalho A, Ziletti A, O'Donnell K M, Koenig S P, Coker D F, Ozyilmaz B, Neto A H C and Fuhrer M S 2015 Creating a stable oxide at the surface of black phosphorus *ACS Appl. Mater. Interfaces* **7** 14557–62

[30] Yuriy Zhirko V T and Kovalyuk Z 2012 On the possibility of layered crystals application for solid state hydrogen storages—InSe and GaSe crystals *Hydrogen Storage* ed P J Liu (Rijeka: Intech) p 213

[31] Zhirko Y, Skubenko N, Dubinko V, Kovalyuk Z and Sydor O 2013 Influence of γ-irradiation on the optical properties of pure or impure Zn, Cd and Ge-doped layered InSe crystals *J. Mater. Sci. Eng.* A **3** 162–74

[32] Drapak S I, Netyaga V V and Kovalyuk Z D 2002 The electrical and photoelectrical properties of n-In2Se3—p-InSe heterostructures *Tech. Phys. Lett.* **28** 711–3

[33] McGuire G E, Schweitzer G K and Carlson T A 1973 Study of core electron binding energies in some group IIIa, Vb, and VIb compounds *Inorg. Chem.* **12** 2450–3

[34] Nelson A J, Swartzlander A B, Tuttle J R, Noufi R, Patel R and Hochst H 1993 Photoemission investigation of the electronic structure at polycrystalline CuInSe$_2$ thin-film interfaces *J. Appl. Phys.* **74** 5757–60

[35] Wagner C D and Muilenberg G E 1979 *Handbook of X-Ray and Ultraviolet Photoelectron Spectroscopy: a Reference Book of Standard Data for Use in X-Ray Photoelectron Spectroscopy* (Eden Prairie, Minn.: Physical Electronics Division, Perkin-Elmer Corp.,) p 55344

[36] Liu W K 1995 Preparation of InSb substrates for molecular beam epitaxy *J. Vac. Sci. Technol.* B **13** 1539

[37] Nelson A J, Gebhard S and Kazmerski L L 1990 Characterization of the native oxide of CulnSe$_2$ using

synchrotron radiation photoemission *Appl. Phys. Lett.* **1428** 1428–30

[38] Madelung O 2003 *Semiconductor: Data Handbook* (London: Springer) p 586

[39] Lang O, Pettenkofer C, Sánchez-Royo J F, Segura A, Klein A and Jaegermann W 1999 Thin film growth and band lineup of In_2O_3 on the layered semiconductor InSe *J. Appl. Phys.* **86** 5687–91

[40] Li L H, Cervenka J, Watanabe K, Taniguchi T and Chen Y 2014 Strong oxidation resistance of atomically thin boron nitride nanosheets *ACS Nano* **8** 1457–62

[41] Karazhanov S Z, Ravindran P, Vajeeston P, Ulyashin A, Finstad T G and Fjellvåg H 2007 Phase stability, electronic structure, and optical properties of indium oxide polytypes *Phys. Rev.* B **76** 1–13